buildings

MDPI

Article

Numerical Investigation of a Multi-Year Sand-Based Thermal Energy Storage System for Building Space Heating Application

Sandeep Bandarwadkar and Tadas Zdankus *

Faculty of Civil Engineering, Kaunas University of Technology, Studentu Str. 48, LT-51367 Kaunas, Lithuania; sandeep.bandarwadkar@ktu.edu

* Correspondence: tadas.zdankus@ktu.lt

Abstract

Residential space heating in Northern Europe requires long-duration thermal storage to align summer solar gains with winter heating demand. This study investigates a compact sand-based seasonal thermal energy storage integrated with flat-plate solar collectors for an A+ class single-family house in Kaunas, Lithuania. An iterative co-design couples collector sizing with the seasonal charging target and a 3D COMSOL Multiphysics model of a 300 m^3 sand-filled, phenolic foam-insulated system, with a 1D conjugate model of a copper pipe heat-exchanger network. The system was charged from March to September and discharged from October to February under measured-weather boundary conditions across three consecutive annual cycles. During the first year, the storage supplied the entire winter heating demand, though 35.2% of the input energy was lost through conduction, resulting in an end-of-cycle average sand temperature slightly below the initial state. In subsequent years, both the peak sand temperature and the residual end-of-cycle temperature increased by 3.7 °C and 3.2 °C, respectively, by the third year, indicating cumulative thermal recovery and improved retention. Meanwhile, the peak conductive losses rate decreased by 98 W, and cumulative annual losses decreased by 781.4 kWh in the third year, with an average annual reduction of 4.15%. These results highlight the progressive self-conditioning of the surrounding soil and demonstrate that a low-cost, sand-based storage system can sustain a complete seasonal heating supply with declining losses, offering a robust and scalable approach for residential building heating applications.

Keywords: residential space heating; seasonal thermal energy storage; sand-based heat storage system; soil thermal interaction; heat loss reduction

Academic Editor: Constantinos A. Balaras

Received: 10 December 2025
Revised: 6 January 2026
Accepted: 9 January 2026
Published: 12 January 2026

1. Introduction

Residential space heating remains a dominant energy demand in the European Union (EU), accounting for approximately 63.5% of household energy consumption in 2022 [1,2]. Despite efforts to transition to renewable energy, fossil fuels play a significant role in meeting this demand. Natural gas alone contributed 30.9% of the final energy consumption in the residential sector, while coal and petroleum products contributed 2.3% and 10.9%, respectively [1]. This heavy dependence on fossil fuels for space heating contributes substantially to greenhouse gas emissions. The construction sector was responsible for 34% of the 2022 energy-related CO_2 emissions of the EU [3]. Addressing this issue is crucial to achieving the EU's climate neutrality goals and enhancing energy resilience. The integration of renewable energy sources, such as wind and solar, into the energy mix has grown significantly, with renewables accounting for 45.3% of the gross electricity

consumption in 2023 [1]. However, the intermittent nature of these sources leads to periods of surplus generation that cannot be effectively utilized without adequate storage solutions. In 2023, the EU wasted the equivalent of 0.5% of its total power consumption due to insufficient storage capacity, highlighting the need for enhanced energy storage infrastructure [4]. Furthermore, studies indicate that to manage extreme droughts of renewable energy, known as 'Dunkelflaute', Europe would require a long-duration storage capacity equivalent to 7% of its annual electricity demand [5]. This finding underscores the vital role of seasonal energy storage systems in ensuring the reliability and efficiency of a renewable-based energy system.

Thermal energy storage technologies are generally grouped into three categories based on the underlying storage principle: sensible, latent, and thermomechanical systems (Figure 1) [6–10]. In sensible storage, thermal energy is retained through a controlled temperature rise in the storage medium, such as water, soil, or sand. Latent storage increases energy density by utilizing the phase-change phenomenon, whereas thermochemical storage relies on chemical sorption processes to store heat with minimal standby losses. For residential applications, the choice of TES technology is primarily constrained by system compactness, feasible operating temperature range, heat-transfer effectiveness, and the ability to limit the thermal losses through appropriate insulation design [7,11].

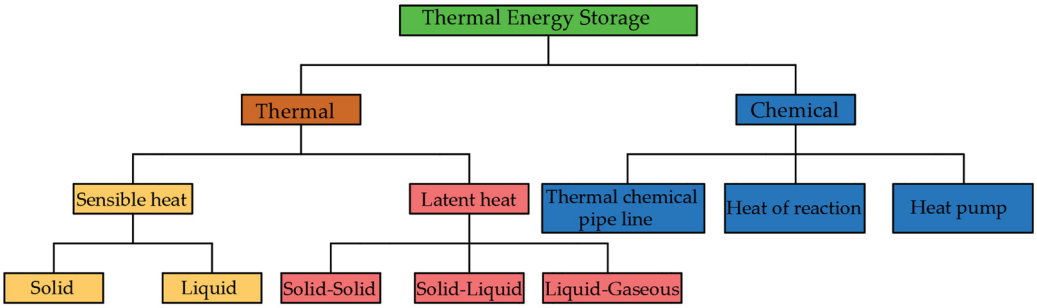

Figure 1. Classification of the TES system based on storage mechanism [7–10].

Seasonal thermal energy storage (STES) systems have been widely investigated through experimental and numerical studies to assess performance and limitations [12–14]. Aquifer thermal energy storage (ATES) stores sensible heat in groundwater aquifers, and optimized control approaches have demonstrated significant reductions in building energy consumption and enhanced resilience to demand variability [15]. However, deployment is constrained by local hydrogeology, contamination risks, and regulatory requirements [16,17]. Borehole thermal energy storage (BTES) stores heat in the subsurface using borehole arrays with U-tube exchangers. Design-control optimization has indicated economic feasibility, including an estimated average household energy cost of approximately EUR 75 per month over a 30-year operating period [18]. However, BTES remains limited by long-term heat losses and substantial land area requirements, particularly in dense urban settings [19]. Thermochemical energy storage (TCES) relies on reversible reactions to achieve high storage density, such as $CaCl_2$ hydration/dehydration tests, which demonstrated good reversibility and cycling stability across 20 cycles within 80–200 °C [20], yet practical implementation is still hindered by slow kinetics, material degradation, and integration complexity [21]. Latent heat storage using phase-change materials (PCMs) provides quasi-isothermal buffering. Cascade PCM configurations can extend the duration of constant thermal power delivery by approximately 65% compared with sensible storage [22]. Despite advances such as microcapsulation to improve thermal performance and reduce leakage [23], PCM-based systems continue to face barriers related to material cost, low thermal conductivity, phase segregation, and long-term reliability [24–26].

Solar energy offers one of the most abundant renewable resources, with applications ranging from electricity production to thermal energy generation for heating and hot water [27]. A key limitation is thermal utilisation. However, lies in the timing mismatch between supply and demand: solar energy peaks in summer, while heating requirements are greatest in the winter months. In summer, solar radiation is plentiful, but the heating load is minimal. Despite this discrepancy, technologies such as flat plate collectors and thermosiphon systems are already widely deployed to meet domestic hot water needs throughout the year. When comparing system efficiencies, flat-plate solar collectors can achieve values close to 80% under water-based operations [28]. Photovoltaic or thermal hybrids reach about 60–65% [29], while crystalline PV modules reach around 28% [30], although this depends strongly on environmental and operational conditions. These efficiency levels highlight that thermal conversion remains highly attractive for building applications, provided that suitable storage is incorporated to capture heat and deliver it when required.

Several studies have specifically examined the use of flat-plate solar collectors as charging units in seasonal thermal energy storage applications. Brites et al. demonstrated that surplus domestic hot water heat from flat-plate collectors can be effectively redirected into seasonal reservoirs, significantly increasing the solar fraction available for space heating in warm and temperate climates [30]. Antoniadis and Martinopoulos used TRNSYS to optimize the sizing of flat-plate collectors and seasonal storage for a single-family dwelling, demonstrating that properly balancing collector area and storage volume can markedly reduce auxiliary energy demand [31]. A validated experimental evaluation by Gado et al. further demonstrated the stable thermal performance of a flat-plate collector when integrated with seasonal thermal storage systems, confirming its suitability for solar-assisted space-heating applications [13]. At a large scale, Yang et al. analysed the deployment of solar-driven seasonal thermal energy storage systems in Heilongjiang, China, reporting that flat-plate collector-based seasonal storage can substantially reduce fossil fuel consumption and improve renewable energy integration in cold climates [32].

Recent efforts have also focused on integrating Seasonal Thermal Energy Storage (STES) systems with renewable energy sources, particularly solar and wind, to enhance load flexibility and reduce dependence on fossil fuels [25,28,29]. In several projects, ATES has been coupled with solar thermal collectors to seasonally shift excess summer heat into the winter space heating, with modeling studies confirming notable reductions in auxiliary heating requirements [33]. However, performance is highly sensitive to system configurations, particularly flow rates and well spacing, which significantly impact thermal breakthrough and storage recovery efficiency [34]. Borehole Thermal Energy Storage (BTES) has shown excellent synergy with solar thermal fields, as demonstrated in the Drake Landing Solar Community in Canada, where integration achieved a 97% annual solar fraction through controlled borehole recharging and discharging sequencing. The key integration challenge in such systems lies in maintaining seasonal thermal balance and preventing thermal drift over multiple years [35,36]. PCM-based systems have also been paired with solar-assisted heating units, where latent heat storage helps stabilize short-term thermal fluctuations. While small-scale trials have confirmed promising storage density and solar energy utilization, integration at the system level is complicated by the need for real-time thermal regulation and stratification control to ensure optimal phase transition behavior [37–39]. In high-temperature applications, Thermochemical Energy Storage (TCES) systems have been considered for use with Concentrated Solar Power (CSP) plants, leveraging the reversible chemical reactions to retain thermal energy over long durations. While simulations report high theoretical round-trip efficiency, integration efforts are still

in the early phase due to challenges in reactor scalability, sorbent regeneration control, and maintaining stable cycling under real-world solar fluxes [40,41].

Although various seasonal storage approaches such as ATES, BTES, latent heat systems, and thermochemical storage have been studied, the literature still lacks a detailed multiyear evaluation of compact, shallow, soil-based sensible TES systems that are directly integrated with solar thermal collectors and operated under realistic climatic and residential heating conditions. Existing work typically examines small prototypes, single-season simulations, or storage concepts that rely on deep boreholes or large water tanks, leaving a gap in understanding how a shallow, sand-filled TES behaves under repeated annual charging and discharging cycles. The present study addresses this gap by developing a fully coupled, three-dimensional numerical framework in COMSOL Multiphysics that models the solar collector field, the 300 m^3 sand-based TES, the surrounding ground, and an A+ class residential building as an integrated energy system. A central contribution of this work is the application of an iterative solar-TES co-design methodology, through which the collector area, TES geometry, and operating strategy are refined based on the evolving thermal behavior of the system. This modelling approach enables, for the first time, a detailed assessment of long-term thermal interactions between the TES and surrounding soil, including the emergence of a thermally conditioned near-field region that modifies local heat transfer behavior over successive years. In doing so, the study provides a technically rigorous and previously unavailable insight into the design and long-term feasibility of compact, low-cost, soil-based seasonal storage solutions for residential heating.

2. Computational Modeling

The methodological workflow adopted in this study is summarized through the following sequential steps: First, the solar thermal collector field was characterized analytically using standard efficiency equations to estimate the useful thermal power and seasonal charging potential. Second, an iterative sizing procedure was carried out to determine the required absorber area, TES volume, insulation thickness, and embedded pipe length based on seasonal energy requirements and preliminary loss estimates. Third, the finalized design parameters were implemented in a coupled 1D-3D COMSOL Multiphysics model, where the pipe network was treated as a 1D consecutive domain and the sand storage region as a full 3D transient conduction domain. Fourth, realistic boundary conditions, including solar input, ambient weather data, ground temperature profiles, and building heating demand, were applied to simulate charging and discharging operations. Finally, the model was run over three consecutive annual cycles, with the temperature field of each year used as the initial for the next. This structured workflow enables a consistent evaluation of storage performance, thermal losses, and long-term soil-TES interactions under realistic operating conditions.

2.1. System Design and Sizing

The present study investigates the seasonal operation of a soil-based thermal energy storage system integrated with solar thermal collectors and coupled to an A+ class residential building in Kaunas, Lithuania (Figure 2). The system is considered within three annual cycles, where storage is charged by solar energy during the warm season (March to September) and discharged to meet the building's space-heating demand during the cold season (October to February). The methodology introduces an explicit treatment of long-term storage behavior by accounting for heat losses during the charging/discharging period and evaluating the extent to which the available storage can satisfy the heating demand in winter.

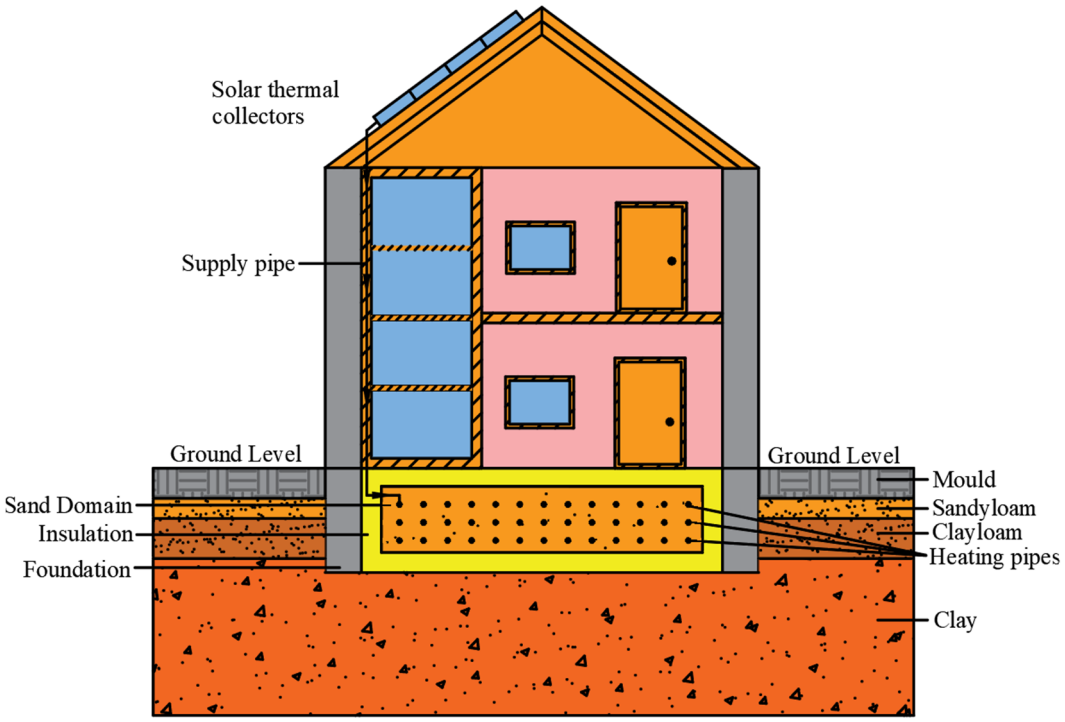

Figure 2. Scheme of sand-based TES below the building coupled with solar thermal collectors for heat storage.

The thermal output of the flat-plate solar collectors was determined analytically based on the parameters summarized in Table 1. The collector characteristics, including geometric dimensions, optical properties, and thermal loss coefficients, were adopted from the certified solar Keymark values. These parameters were applied in the standard efficiency equation defined by ISO 9806 [42], which relates incident solar irradiance, optical efficiency, and heat loss coefficients to the useful collector output. Representative solar irradiance data for Kaunas, Lithuania, were obtained from the PVGIS database developed by the Joint Research Center of the European Commission [43]. The dataset provides the normal irradiance (DNI), diffuse horizontal irradiance (DHI), and the resulting global tilted irradiance (GTI) for a 40° south-facing surface. For Kaunas (54.8834° N, 23.8349° E), the typical annual GTI ranges between 1150 and 1250 kWh/m^2, with DNI contributing approximately two-thirds and DHI one-third of the total [44,45]. These values were used directly in the calculation of the collector's thermal power. During the dark period, the solar irradiance is zero, and fluid circulation through the collector is therefore interrupted. As a result, the collector fluid cools to near-ambient temperature due to environmental losses. This control strategy prevents reverse heat transfer from the TES back to the environment, reflecting the practical operation of solar thermal systems.

Table 1. Flat-plate solar collector parameters used in the study [46–48].

Parameter	Value	Symbol	Unit
Gross collector area	2.0	A_{gross}	m^2
Aperture/absorber area	1.8	A_{abs}	m^2
Tilt angle	40	β	Degree
Azimutrh (south = 0)	0	γ	Degree
Absorptance	0.95	τα	-
Emittance	<0.10	ε	-
Glazing transmittance	0.90	τ_{glass}	-
Insulation thermal conductivity	0.035	$\lambda_{coll,ins}$	W/m·K

Table 1. *Cont.*

Parameter	Value	Symbol	Unit
Optical efficiency	0.76	η_o	-
First-order loss coefficient	4.07	a_1	$W/m^2 \cdot K$
second-order loss coefficient	0.02	a_2	$W/m^2 \cdot K^2$
Mean temperature difference	45	$\Delta T_{c\text{-}a}$	K
Operating-point efficiency	0.53	η_{coll}	-
Reference irradiance	1000	G_{ref}	W/m^2

A seasonal sizing relation was applied to determine the absorber area required to charge the TES. The gross charging requirement, E_{target}, includes both the useful building demand and the thermal losses of the TES, which are quantified through simulations. The collector area at iteration *n* was expressed in Equation (1).

$$A^n_{coll,total} = \frac{E^n_{target}}{\eta_{coll} E_s} \quad (1)$$

where $A^n_{coll,total}$ is the total Absorber area of the collector field at iteration n (m^2), E^n_{target} is the gross seasonal charging requirement at iteration n (kWh), E_s is the cumulative tilted irradiation over the charging season (kWh/m^2).

The minimum number of collectors (N_{coll}) required in the solar field was then determined using Equation (2).

$$N_{coll} \geq \frac{A^n_{coll,total}}{A_{abs}} \quad (2)$$

Since the actual TES losses are unknown beforehand, the gross seasonal charging requirement was determined iteratively using Equation (3). After each simulation, the seasonal losses were calculated and added to the building demand to update the requirement accordingly.

$$E^{n+1}_{target} = E_b + E^n_{loss} \quad (3)$$

where E_b is the heating demand of the building (kWh), E^n_{loss} is the seasonal TES losses obtained from the nth simulation (kWh).

The useful thermal power of the collector field is given in Equation (4) below.

$$P_{coll}(t) = N_{coll} A_{abs} \left[\eta_o G(t) - a_1 (T_{f,m}(t) - T_a(t)) - a_2 (T_{f,m}(t) - T_a(t))^2 \right] \quad (4)$$

where $G(t)$ is the global irradiance on the tilted plane of 40° (W/m^2), η_o is the optical efficiency given in Table 1 (-), a_1 is the first-order thermal loss coefficient given in Table 1 ($W/(m^2 \cdot K)$), a_2 is the second-order thermal loss coefficient given in Table 1 ($W/m^2 \cdot K^2$), $T_{f,m}(t)$ is the mean fluid temperature in the collector (($T_{coll,flu,out}(t) + T_{coll,flu,in}(t)/2$), (K), $T_{coll,flu,out}(t)$ is the time-dependent collector outlet temperature (K), $T_{coll,flu,in}(t)$ is the time-dependent collector inlet temperature (K), $T_a(t)$ is the ambient air temperature (K).

The heated working fluid in the solar collectors subsequently transports the captured thermal energy to the underground TES. A water-propylene glycol mixture with a 33.3% concentration was selected as the heat transfer medium, as it provides stable operation under varying climatic conditions [49]. The fluid has a density of $\rho_{fl} = 1034$ (kg/m^3) and a specific heat capacity of $C_{p,f} = 3600$ ($J/(kg \cdot K)$). The circulation loop operates at a system pressure of four bars, with a total fluid volume of 19.8 L and an average volumetric flow rate of $\dot{v} = 288$ (L/h) [50]. The simultaneous energy rise (ΔT_f) in the circulating fluid from

the collector output and carried to the TES domain, assuming that all the useful heat gained by the absorber is transferred to the fluid stream, is given in Equation (5).

$$\Delta T_f = T_{coll,flu,out}(t) - T_{coll,flu,in}(t) = \frac{P_{coll}(t)}{\dot{v}\rho_{fl}C_{p,f}} \quad (5)$$

The volume of the heat storage (TES) is directly related to the maximum amount of heat that must be charged into the accumulator. The sand with humidity (μ_{sand} = 10%), density (ρ_{sand} = 1800 kg/m^3), and heat capacity ($C_{p,sand}$ = 1200 J/(kg·K)) was selected as the storage medium. The change in the storage temperature is a crucial parameter for the long operation of the thermal storage system. Excessive temperature increase leads to greater heat losses through the surrounding boundaries of TES, while too small a temperature difference limits the storage capacity. Therefore, in this research, the design temperature rise was assumed to be $\Delta T = 50 \pm 2.5$ °C to maintain a practical balance between stored energy and thermal losses. The storage volume (V^n_{sand}) was evaluated (Equation (6)) from the sensible-heat retention using the iteratively defined seasonal charging requirement.

$$V^n_{sand} = \frac{E^n_{target}}{\rho_{sand}C_{p,sand}\Delta T} \quad (6)$$

where ρ_{sand} is the density of the sand (kg/m^3), $C_{p,sand}$ is the specific heat of the sand (J/(kg·K)), ΔT is the temperature difference between the maximum storage temperature and its initial equilibrium ground temperature (K).

To ensure that the designed thermal energy storage (TES) volume can be effectively charged and discharged, the embedded pipe network must provide sufficient heat transfer capacity. To achieve the required heat exchange intensity, both the materials and the pipe dimensions were carefully selected. Copper was chosen for its high thermal conductivity, which supports efficient heat transfer between the circulating heat transfer fluid and the surrounding sand [51]. The selected pipe was DN20 with a wall thickness of 1 mm (inner diameter d_1 = 0.02 m, outer diameter d_2 = 0.022 m). Under the assumed laminar flow regime, the internal heat transfer coefficient from the fluid to the pipe wall was approximately h_1 = 70 (W/(m^2·K)). These properties were included in the COMSOL model to capture the coupled conduction process within the system. The required pipe length (L_{pipe}) was then estimated from Equation (7).

$$L^n_{pipe} = \frac{1}{\pi} \frac{P^n_{TES}}{\left[\left(\frac{1}{h_{in}d_1} + \frac{1}{2\lambda_{cu}}\ln\frac{d_2}{d_1}\right)\right]^{-1}\left(T_{f,m} - T_{avg,sand}\right)} \quad (7)$$

where λ_{sand} is the thermal conductivity of the sand (W/(m·K)), $T_{avg,sand}$ is the average temperature of the sand in TES (K).

All the generated solar heat is delivered to the underground storage through the buried pipe network. The thermal power stored (P_{TES}) in the sand over the charging interval can be calculated by Equation (8).

$$P_{TES}(t) = \frac{1}{t}\rho_{sand}V^n_{sand}C_{p,sand}\left(T_{sand,t_{(j+1)}} - T_{sand,t_{(j)}}\right) \quad (8)$$

where $T_{sand,t_{(j+1)}}$; $T_{sand,t_{(j)}}$ is the soil temperature at jth and j + 1th moment of time t (K).

In underground thermal energy storage, the surrounding ground acts as a continuous heat sink, and without protective measures, seasonal charging would dissipate before the energy could be recovered. To suppress this long-term leakage, the TES was enclosed on all four sides with a thermal insulation layer. An initial estimate of insulation thickness (δ^1_{ins})

was obtained by constraining conductive losses to the allowable design margin. Using a steady-state conduction approximation, the starting thickness was calculated by using Equation (9).

$$\delta_{ins}^{1} = \frac{\lambda_{ins} A_{total} \Delta T t_{charge}}{\varnothing_{max} E_b} \quad (9)$$

where $\varnothing_{max} E_b$ is the maximum tolerable seasonal loss, expressed as a fraction of the building demand E_b (kWh), λ_{ins} is the thermal conductivity of insulation (Phenolic foam) (W/m·K), A_{total} is the total insulated surface area (m^2), t_{charge} is the duration of the storage period considered for heat loss (s), $\varnothing_{max}$ is the maximum allowable seasonal loss fraction, a design constraint, often taken as 0.20–0.30 of the building demand, following [52].

For each candidate thickness (δ_{ins}^{n}), the annual cycle was simulated, and the seasonal loss fraction (η_{loss}^{n}) was evaluated using Equation (10).

$$\eta_{loss}^{n} = 1 - \frac{P_{TES}(t)}{P_{coll}(t)} \quad (10)$$

The gross seasonal charging requirement was then updated iteratively in Equation (3), where E_{loss}^{n} is given in Equation (11)

$$E_{loss}^{n} = \eta_{loss}(n) \int_{t_0}^{t_f} P_{coll}(t) dt \quad (11)$$

where t_0 is the start time of the charging (s), t_f is the finish time of the charging (s).

2.2. Numerical Simulation Using COMSOL Multiphysics

The numerical model was implemented in COMSOL Multiphysics version 6.1. The three-dimensional sand domain was simulated using the Heat Transfer in Solids interface. At the same time, the embedded pipe network was represented using a coupled one-dimensional heat transfer-in-pipes formulation, ensuring continuity of temperature and heat flux at the pipe-sand interface (Figure 3). The governing equations were discretized spatially using the finite element method (FEM). Transient simulations were performed using COMSOL's time-dependent solver, which employed an implicit backward differentiation formula (BDF) scheme with adaptive time stepping. Nonlinearities arising from temperature-dependent coupling were resolved using a Newton-Raphson method, and the resulting linear systems were solved using COMSOL's default sparse direct solver (PARDISO). The final design parameters summarized in Table 2 were applied as boundary and initial conditions to simulate TES dynamics and thermal losses throughout the charging and discharging cycles.

Table 2. Final design parameters.

Parameters	Symbol	Value	Unit
Total collector absorber area	$A_{coll,total}$	17.8	m^2
Number of flat-plate collectors	N_{coll}	10	units
TES volume	V_{sand}	300	m^3
Design Temperature swing	ΔT	50 ± 2.5	C
Insulation thickness	δ_{ins}	0.25	m
Total pipe length	L_{pipe}	390	m

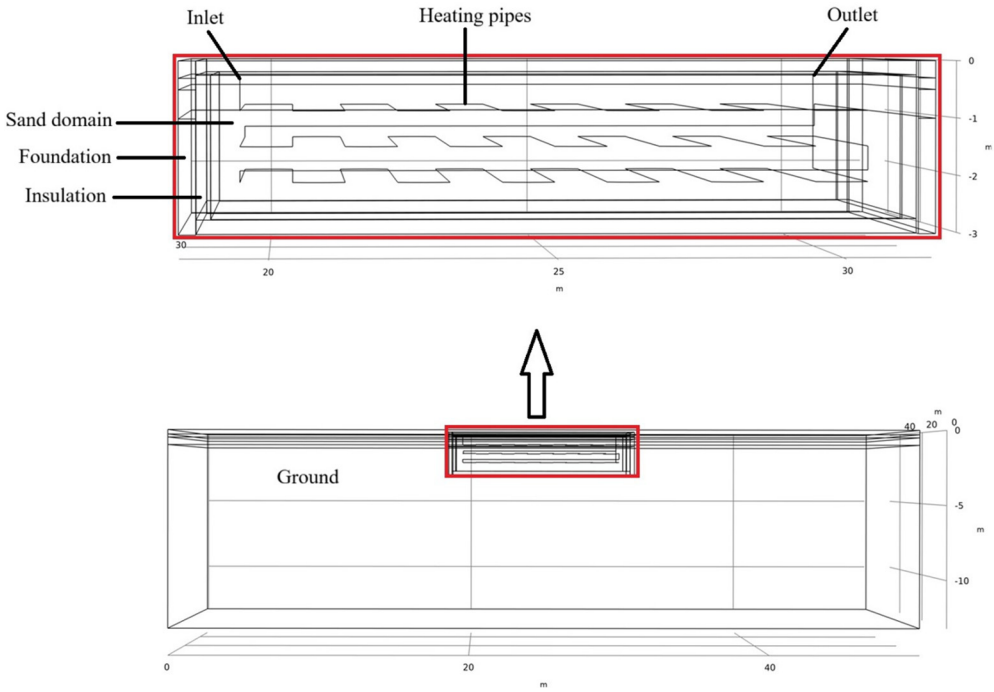

Figure 3. COMSOL model of sand-based TES used for numerical simulation.

A three-dimensional sand domain measuring 12 m in length, 10 m in width, and 2.5 m in depth, computing the total volume of V_{sand} = 300 m^3, was constructed in COMSOL. A 0.3 m thick concrete foundation was included to support the building floor, and the entire foundation was enclosed with a 0.25 m thick insulation of phenolic foam to minimize heat losses. The insulated cavity was filled with sand, which served as the primary storage medium. The thermal behaviour of the sand was governed by a transient heat-conduction equation, which describes the temporal variation in internal energy together with conductive redistribution across the sand layers. Equation (12) represents transient heat conduction in the sand-based TES formulated according to Fourier's law for a homogeneous medium, which reflects the non-uniform heating characteristics of the TES, where near-surface regions respond quickly to heating, intermediate depths regulate the transfer rate, and the deep layer acts as a long-term reservoir.

$$\rho_{sand} C_{p,sand} \frac{\partial T_{sand}}{\partial t} = \nabla \cdot (\lambda_{sand} \nabla T_{sand}) + Q \quad (12)$$

where T_{sand} is the temperature field within the sand domain (K), t is the time representing the transient simulation (s), $\nabla \cdot (\lambda_{sand} \nabla T_{sand})$ is the conductive heat flux (W/m^3), Q is the volumetric heat source (W/m^3).

The numerical approach employed in this study follows the same modelling methodology previously validated in an experimental-numerical investigation. In that work, soil temperature evolution and heat flux behaviour were measured and compared with COMSOL Multiphysics simulations, and good agreement was achieved under both steady and transient conditions. Although the present test model uses a different geometric configuration and boundary conditions, the physical formulation, including transient heat conduction in soil, material definitions, and numerical solution strategy, is identical. Therefore, the prior experimental comparison provides validation for the modelling framework applied here, confirming that the approach reliably represents soil heat-transfer processes relevant to seasonal TES [53].

In addition to the vertical redistribution of heat between adjacent layers within the storage volume, part of the energy is inevitably dissipated through the external boundaries

of the TES into the surrounding ground. The relative share between inter-layer transfer and the boundary leakage is determined by the effective thermal resistance along the two pathways. While inter-layer conduction is governed by the intrinsic conductivity of the filler and discretization depth, boundary leakage depends on the resistance of the insulation layer in series with that of the adjacent soil. This representation enables explicit quantification of the seasonal heat losses ($Q_{loss}(t)$) through the insulating envelope as a function of insulation thickness and material properties. The heat loss rate at different times is calculated using Equation (13).

$$Q_{loss}(t) = \int_0^{A_b} \left(\frac{\lambda_{ins}}{\delta_{ins}} + \frac{\lambda_g}{\delta_g} \right) \left(T_{avg,sand}(t) - T_g(t) \right) dA_b \quad (13)$$

The corresponding cumulative seasonal heat loss ($Q_{cumulative\ loss}$) is obtained using Equation (14).

$$Q_{cumulative\ loss} = \int_0^t Q_{loss}(t) dt \quad (14)$$

where A_b is the total boundary surface area (m^2), $T_{avg,sand}(t)$ is the average temperature of the sand at time t (K), $T_g(t)$ is the external ground temperature at time t (K), δ_g is the effective conduction distance through the surrounding ground (m), λ_g is the thermal conductivity of the surrounding ground (W/(m·K)).

All the generated solar heat was transferred into the accumulator via the pipe network. The selected copper pipe was arranged in three horizontal layers within the storage volume to ensure uniform heat distribution. The layers were positioned at depths of 0.625 m, 1.25 m, and 1.875 m below the upper boundary of the storage cavity. Within each layer, pipes were spaced 1 m apart and bent with a turning radius of 1 m to ensure practical installations and acceptable hydraulic resistance [54]. The inlet and outlet manifolds were positioned near the top of the storage, with their connections at a level of 0.3 m below the surface, ensuring that the supply and return lines could be integrated without disturbing the upper insulation and floor slab. This configuration yielded a total effective pipe length of 390 m, resulting in improved exchanger effectiveness, mitigating local thermal gradients, and enhanced robustness under seasonal variations, while remaining hydraulically feasible [51]. This arrangement was implemented in the COMSOL model to resolve transient conduction-convection coupling between the circulating fluid and sand filler. Table 3 lists the adopted thermophysical parameters for soil layers, insulation, and the copper pipe network.

Table 3. Thermophysical parameters of soil layers in the ground, insulation, and pipe network [55–58].

Material	Thermal Conductivity [W/(m·K)]	Density [kg/m^3]	Specific Heat Capacity [J/(kg·K)]
Mould	0.45	1300	1800
Sandyloam	1.20	1600	850
Clayloam	0.55	1400	1400
Clay	0.80	1900	1500
Phenolic foam (Insulation)	0.018	40	1400
Copper pipe	390	8960	385
Sand (filler)	1.45	1800	1200

The thermal behaviour of the circulating fluid inside the embedded pipe network, the governing balance was formulated along the pipe centreline. This one-dimensional

(1D) treatment allows the small-diameter piping to be coupled with the three-dimensional (3D) storage domain without incurring prohibitive meshing requirements. The balance incorporates transient energy accumulation in the fluid, convective transport along the pipe, conductive redistribution through the pipe wall into the surrounding sand, and hydraulic dissipation expressed via a Darcy-Weisbach friction term. Convective heat transport along the pipe centerline is given by the axial mean flow velocity, where the tangential velocity u_t used in the 1D formulation is taken equal to the axial velocity u. Heat exchange between the pipe fluid and the surrounding sand is implemented through the pipe wall as distributed heat flux, providing two-way thermal coupling between the 1D pipe domain and the 3D solid storage domain while ensuring continuity of temperature and heat flux at the pipe-sand interface. Hydraulic losses are evaluated using the Darcy friction factor f_D, which is defined based on the flow regime, under laminar flow conditions $f_D = \frac{64}{R_e}$, where the Reynolds number is given by $R_e = \rho_{fl} u d_h / \mu$. The governing energy equation is given in Equation (15).

$$\lambda_f \frac{\partial^2 T_{f,pipe}}{\partial x^2} + \frac{1}{2} f_D \frac{\rho_{fl}}{d_h} |u| u^2 = \rho_{fl} C_{p,f} \frac{\partial T_{f,pipe}}{\partial t} + \rho_{fl} C_{p,f} u_t \frac{\partial T_{f,pipe}}{\partial x} \quad (15)$$

where $T_{f,pipe}$ is the fluid temperature along the pipe axis (K), x is the axial coordinate along the pipe (m), λ_f is the thermal conductivity of the fluid (W/(m·K)), f_D is the Darcy friction factor (-), d_h is the hydraulic diameter of the pipe (equal to inner diameter for circular pipes) (m), u is the average fluid velocity along the pipe (m/s), $|u|u^2$ is the momentum-dependent frictional dissipation (m^3/s^3), $C_{p,f}$ is the specific heat capacity of the fluid (J/(kg·K)), u_t is the tangential velocity for convective transport (m/s), μ is the dynamic viscosity with a value (3-5) $\times 10^{-3}$ (Pa·s) for a propylene water-glycol mixture.

3. Results

The annual space heating demand of the selected A+ energy class single-family dwelling, with a heated floor area of 120 m^2, was calculated using the Heating Degree Day (HDD) approach based on the monthly average outdoor data representative of Kaunas climatic conditions. The HDD method was selected because it offers a robust climate-based estimate of seasonal heating demand and is commonly used in long-term TES studies where the interest lies in seasonal rather than short-term load dynamics [59]. Converting monthly demand into a continuous daily profile smooths short-term fluctuations and cannot reproduce intra-day variability or peak loads; however, this level of discretization remains appropriate for seasonal TES analysis, where system-level performance is driven primarily by multi-month thermal behaviour and cumulative annual energy balances [60,61]. The building envelope meets the requirements of STR 2.01.02.2016 for A+ energy class performance, with representative U-values of 0.11 W/(m^2·K) for exterior walls, 0.09 W/(m^2·K) for the roof, 0.13 W/(m^2·K) for the ground-contact slab, and 0.85 W/(m^2·K) for high-performance triple glazing. These specifications correspond to an overall heat loss coefficient of approximately 0.38 W/(m^2·K) when ventilation and thermal bridges are included. The model assumes a steady indoor temperature of 20 °C, supplied through a low-temperature hydronic distribution system, consistent with seasonal TES operation. The subsurface TES is located beneath the building, and accommodating sand storage volume within the insulation layer and overhanging foundation on each side yields an effective building footprint of approximately 145 m^2. Although larger than the national average functional dwelling area of 68.4 m^2, this scale remains within the typical upper range of modern detached houses in Lithuania, where private ownership accounts for nearly 98.6% of the housing stock [62,63]. Hence, the selected case represents a realistic upper-bound scenario for a modern, energy-efficient family house in Kaunas. The resulting monthly

heating demand shows a steady increase from October, reaching its maximum in December and January, and then declining toward March. The total space-heating requirement for the cold season amounts to approximately E_b = 6459 kWh (Figure 4), which corresponds well with measured data for an A+ class building in similar climatic conditions [63,64]. To accurately represent this behaviour in the numerical model, the monthly heating demand values were temporally discretized over each month to obtain a continuous daily heating load function. This time-dependent load was then implemented as a boundary heat extraction condition in COMSOL during the discharge phase, allowing the simulation to replicate the real dynamic interaction between the buildings' variable heating requirements and the thermal energy released from the storage system.

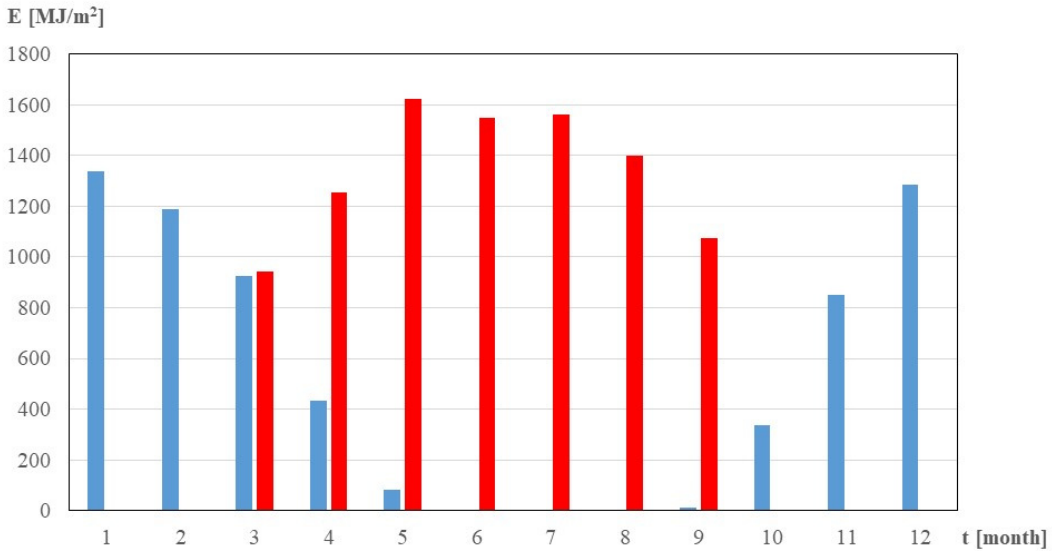

Figure 4. Monthly collector energy (red) and building heating demand (blue) for an A+ building in Kaunas, Lithuania.

The solar thermal collector system was employed as the exclusive heat source for charging the soil-based thermal energy storage unit. The specifications of the collector field are given in Table 1. The collectors were mounted at a 40° inclination, corresponding to the latitude of Kaunas (54.9° N). For fixed flat-plate collectors, global analyses demonstrate that the optimum annual tilt for maximizing the annual irradiance lies close to site latitude, or slightly adjusted depending on climate and seasonal distribution conditions. In the present study, where charging is limited to the warmer months, a 40 tilt therefore provides a balanced trade-off between optical efficiency during spring-autumn and realistic installation geometry [65–67]. The TES charging was set from March to September, when solar altitude and daily irradiance levels are sufficiently high to ensure effective heat collection. During this period, the system operates under the favorable solar geometry and extended daylight hours, enabling stable thermal input to the storage. In contrast, from October to February, the solar elevation angle remains low, typically below 20° in Kaunas, and the combination of short days, low irradiance, and frequent cloud cover results in minimal collector output, making winter months unsuitable for seasonal charging [68]. Throughout the March-September period, the monthly solar energy incident on the collector surface varied between 355 and 612 MJ/m^2, yielding a cumulative irradiation of 3548 MJ/m^2 corresponding to E_s = 985.6 kWh/m^2 (Figure 4). Considering the collector area and efficiency, the total thermal energy supplied to TES amounted to E^n_{target} = 9402 kWh. In the simulation, the solar energy input was represented as a continuous, time-dependent thermal function, derived by distributing the monthly irradiation over its respective duration. This function was applied at the collector-TES interface in COMSOL.

The numerical simulation was initiated in March, corresponding to the onset of the TES charging season. The initial ground temperature distribution with depth was defined using the Kusuda-Achenbach periodic ground temperature model, which describes the annual variation in soil temperature with exponential damping in depth, consistent with EN ISO 13370's [69] treatment of periodic ground heat flow for building elements in contact with ground. For Kaunas, the climatic values were obtained from the ASHRAE 2021 meteorological dataset embedded in COMSOL's Ambient Properties module, corresponding to the Kaunas weather station (No. 266290, 54.8834° N, 23.8349° E, 77 m above the sea level). The ambient conditions, including outdoor dry-bulb air temperature, dew-point temperature, wind speed, and precipitation rate, were sourced from this station and applied as time-dependent variables throughout the simulation period. This ensured a realistic coupling between the subsurface thermal field and the external climatic environment of Kaunas.

At the upper boundary, representing the interface between the sand layer and overlying insulation, an adiabatic boundary condition was applied. This condition assumes zero heat flux across the surface, based on the rationale that any upward heat released from the TES contributes to the thermal balance of the building above rather than being lost to the ambient environment. The initial temperature of the sand filler was assigned as $T_{avg,\,sand}$ = 20.0 °C, representing a physically justified assumption of the mean pre-heating temperature of the storage medium at the beginning of the charging period. This provides a stable baseline for simulating the subsequent charging and discharging cycles, reflecting the average thermal state of the soil mass before active solar input begins.

At the beginning of the simulation, the average sand temperature was $T_{avg,\,sand}$ = 20.1 °C (Figures 5 and 6), while the surrounding soil temperature followed the natural ground temperature profile representative of March in Kaunas. The heat loss rate (Equation (13)) at this stage was Q_{loss} = 229.9 W (Figure 5), representing weak conductive exchange between the TES and the cooler surrounding soil. The temperature field at t = 0 d shows almost a uniform temperature distribution, confirming that the system initially contained no stored thermal gradients. Once solar energy began, the supplied energy was absorbed mainly by the inner sand layers, while the outer boundaries remained close to the initial temperature. As a result, the heat loss rate changes only marginally in this early phase. With continued charging, the stored energy accumulated progressively, and the temperature difference between the TES and the surrounding soil increased. By t = 122 d, the average sand temperature reached $T_{avg,\,sand}$ = 46.7 °C, and the temperature field (Figure 6) illustrates the formation of a thermal front, a distinct region of elevated temperatures extending laterally and downward into the adjacent sand layers. This expansion of the heated zone increased the thermally affected volume and strengthened conduction through the sides and base, causing a marked rise in the heat loss rate of Q_{loss} = 538.3 W.

The maximum heat loss of Q_{loss} = 685.5 W occurred at t = 193 d, when the average sand temperature was at the peak of $T_{avg,\,sand}$ = 59.0 °C (Figure 5). The temperature field at this stage (t = 183 d) shows that the upper part of the sand layer contained the highest temperature, forming a concentrated hot zone beneath the insulated interface, while the sides and bottom regions exhibited lower temperatures where heat was conducted toward the surrounding ground. This temperature stratification produced the strongest lateral and vertical gradients, resulting in the peak conductive heat flux. After this point, the system approached the quasi-steady condition, as the rate of energy gain and loss became comparable.

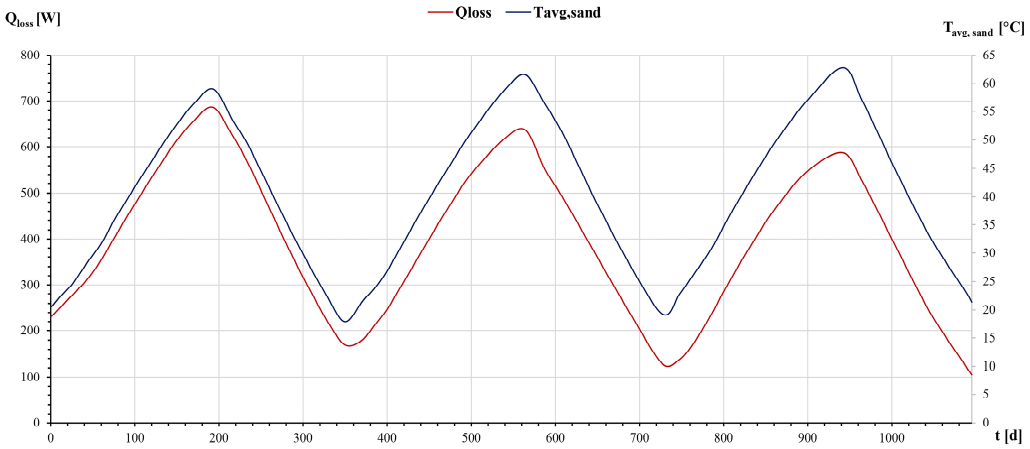

Figure 5. Variation of heat loss rate (red) of the TES and an average sand temperature (blue) over three consecutive years.

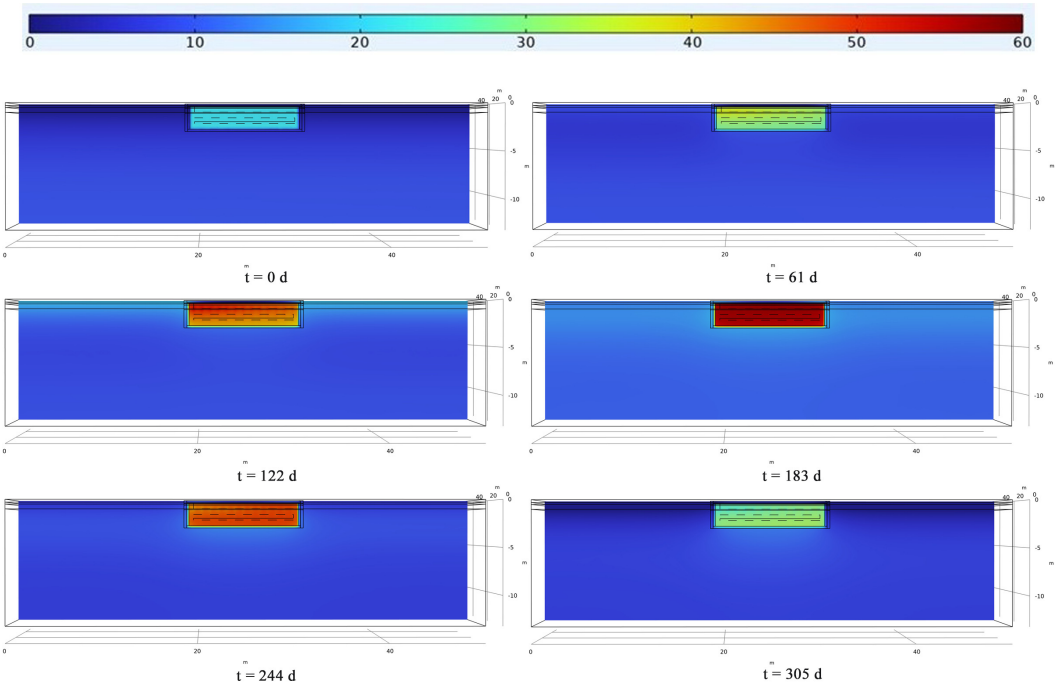

Figure 6. Temperature field evolution in the sand-based TES at different time intervals during the charging and discharging cycle of the first year simulation.

A potential concern in seasonal subsurface thermal energy storage is the influence of elevated summer storage temperatures on indoor thermal comfort. In the present system, this effect is mitigated by the complete enclosure of the sand-based TES with a 0.25 m thick phenolic foam insulation layer, which provides high thermal resistance and effectively decouples the storage from the occupied space above. Heat transfer toward the building occurs only by conduction and is strongly attenuated by the insulation and floor slab, resulting in slow, diffusive heat transfer with short-term temperature peaks. Since TES charging occurs on a seasonal timescale, while indoor comfort is governed by short-term gains and ventilation, the elevated sand temperatures during summer do not cause measurable increases in indoor air temperature or deterioration of occupant thermal comfort.

After the temperature peak, the TES continued to receive solar input during the final stage of the charging period. During this period, the available solar irradiance gradually decreased compared with the preceding summer months, resulting in reduced thermal

energy input from the collector field. As the TES had already attained a high temperature, the driving thermal gradient for further charging became smaller, which limited the amount of additional heat that could be absorbed. Consequently, a portion of the supplied energy was spent compensating for conductive losses and redistributing heat within the sand volume, leading to a slight decline in the average temperature of the sand reaching $T_{avg,\ sand}$ = 56.8 °C by t = 213 d.

The temperature field at t = 244 d shows the discharging phase, when stored energy was gradually supplied to the building for heating. The average sand temperature at this stage was $T_{avg,\ sand}$ = 46.3 °C, and the heat loss rate had decreased to Q_{loss} = 528.5 W. The upper sand region had already begun cooling more rapidly due to continuous heat extraction, while the middle and lower zones retained higher temperatures. This inversion of the vertical temperature gradient marks the shift from heat accumulation to controlled release. Between t = 244 d and 305 d, the average sand temperature declined further from $T_{avg,\ sand}$ = 46.3 °C to $T_{avg,\ sand}$ = 28.6 °C, while the heat loss rate dropped from Q_{loss} = 528.5 W to Q_{loss} = 301.4 W, respectively. The temperature field at t = 305 d shows that the upper and near-surface layers cooled quickly, influenced by both heat supply to the building and enhanced convective cooling of the ground surface under winter conditions, characterized by low ambient air temperature and higher wind velocity. Conversely, the bottom layers experienced much slower cooling, as heat dissipation there was governed by gradual conduction through the underlying soil.

This simultaneous contrast- rapid cooling at the upper zone and slow dissipation at depth, created a reverse vertical temperature gradient, opposite to that formed during the charging. The TES thus behaved as a progressively depleting heat reservoir, releasing energy sequentially from the upper to lower layers. By t = 365 d, the average sand temperature has fallen to $T_{avg,\ sand}$ = 18.1 °C (Figure 5), and the heat loss rate reached Q_{loss} = 174.5 W, confirming that the stored energy had been utilized for building heating. The slightly lower average temperature of the sand at the end of the first cycle is attributed to continued conductive heat loss to the surrounding soil during the discharge phase. While most of the stored energy was supplied to the building for heating, a smaller fraction continued to dissipate through the side and bottom boundaries, resulting in a minor reduction in the residual temperature of the sand by the end of the year. The cumulative heat loss during the first year, calculated using Equation (14), reached 3309.5 kWh, 35.2% loss (Equation (10)).

Following the completion of the first annual cycle, the TES simulation was extended for two additional operational cycles, using the final temperature field of each cycle as the initial condition for the subsequent one. During the second year cycle, the maximum average sand temperature increased to $T_{avg,\ sand}$ = 61.4 °C by t = 564 d, while the corresponding peak heat loss rate decreased to Q_{loss} = 636.5 W compared with the previous cycle. This combination of higher internal temperature and lower heat flux indicates that as the surrounding soil warmed from the preceding operation (Figure 7), the temperature gradient at the TES boundaries decreased, reducing conductive leaks to the ground. Consequently, a greater fraction of the supplied solar energy was retained inside the storage instead of reheating the peripheral soil. At the end of this cycle. The average sand temperature increased to 19.6 °C, slightly higher than that of the first cycle, indicating a small but measurable improvement in residual heat retention. The cumulative heat decreased to 2924.0 kWh (31.1%) compared to the first year's cycle.

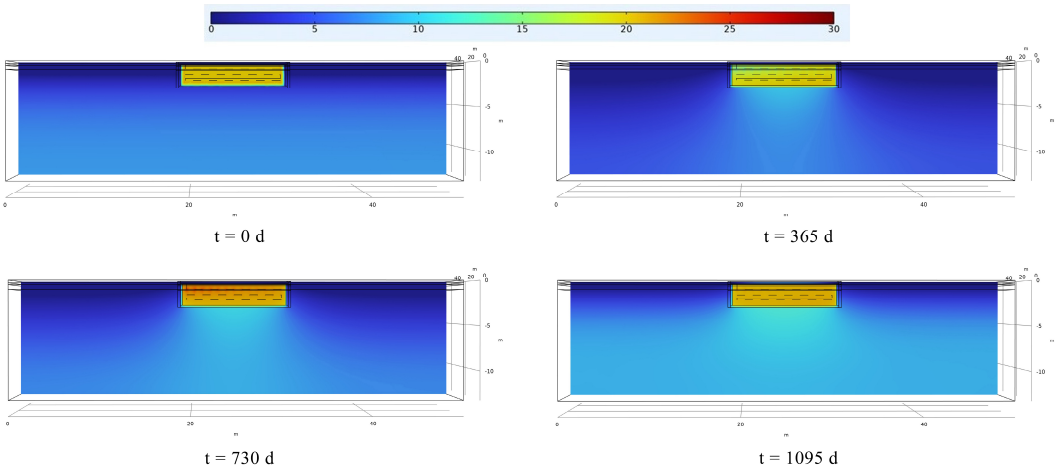

Figure 7. Temperature distribution within the TES and surrounding soil at the end of each annual cycle over three consecutive years.

In the subsequent cycle, the peak average sand temperature rose further to $T_{avg,\,sand}$ = 62.7 °C by t = 941 d, with a maximum heat loss rate of Q_{loss} = 587.5 W. The cumulative heat loss for this cycle was 2529.1 kWh (26.9%), confirming continued improvement in thermal retention. The obtained peak sand temperatures of 59.0–62.7 °C fall within the typical operating range reported for solar-charged seasonal thermal energy storage systems used for low-temperature space heating. Likewise, the predicted annual conductive heat loss fractions of 35.2% in the first cycle and 26.9% after thermal conditioning are consistent with values reported for shallow and insulated subsurface TES systems, where losses strongly depended on insulation strategy, geometry, and climatic conditions. The observed trend of decreasing losses over successive years is therefore physically consistent with independent literature data [7,14,19]. The average sand temperature reached 21.3 °C at the end of this cycle, showing a gradual upward shift in the baseline storage temperature. This behavior reflects the establishment of a thermally conditioned zone around the TES (Figure 7), where the surrounding soil maintains a moderately elevated temperature compared to deeper, undisturbed layers.

4. Economic Analysis of Proposed Sand-Based TES

A simplified cost comparison was conducted to highlight the economic position of the sand-based TES proposed in this study relative to a conventional water-based seasonal storage operation, such as tank-type TES (TTES), and aquifer TES (ATES). Sand storage is structurally simple and relies on locally available backfill material, with typical sand prices of €10–20 per m^3 as reported by the EU construction aggregate market [70]. Phenolic foam insulation is commercially priced at €180–250 per m^3 according to European insulation manufacturers [71]. Including excavation and embedded piping, typical European installation cost databases indicate that 300 m^3 sand TES can be constructed for approximately €12,000–18,000, depending on local labor and soil conditions [72].

In contrast, TTES systems require pressurized or reinforced tanks, corrosion-resistant lining, stratification management, freeze protection, and periodic maintenance. For a thermodynamically consistent comparison, the cost assessment must be based on equivalent thermal energy rather than equal storage volume. Due to the significantly higher volumetric heat capacity of water, an energy storage capacity equivalent to the 300 m^3 sand-based TES investigated in this study can be achieved with a water tank volume of approximately 100 m^3 for a comparable operating temperature range. International assessment from IEA-ETSAP and IRENA shows TTES costs of €150–300 per m^3, translating to €15,000–30,000

for an energy-equivalent water-based seasonal storage system [73]. ATES installations, while not requiring tanks, involve hydrogeological investigation, drilling, groundwater permitting, pumping infrastructure, and monitoring systems. Multiple European studies report ATES capital investments in the range of €100,000–250,000, making such systems viable mainly at the district scale [74].

Borehole Thermal Energy Storage systems require drilling of a borehole equipped with U-tubes, and their cost is dominated by drilling depth and geological conditions. European solar-district-heating data indicate a typical drilling cost of €50–80 per meter of borehole, depending on soil/rock hardness and field configuration [75]. For large seasonal systems, cost analysis from completed projects shows total BTES field investment commonly exceeding €150,000, as reported in international TES cost comparisons [76]. These higher capital requirements, combined with land area needs, place BTES economically closer to ATES.

5. Conclusions

This study presents a detailed multi-year numerical investigation of a soil-based thermal energy storage system integrated with solar thermal collectors, developed through an iterative methodology that coupled insulation design, solar energy availability, and long-term heat loss evaluation. Over the simulated three-year operation, the TES exhibited clear evidence of progressive thermal adaptation. The surrounding soil gradually warmed, acting as a secondary heat sink that reduced the boundary temperature gradients and mitigated the conductive losses. Concurrently, in the simulated temperature fields, a vertical thermal stratification pattern was observed, with heat predominantly concentrated in the upper sand layers during charging and gradually extending downward as the storage volume warms. During discharging, the temperature distribution reversed smoothly, allowing sequential and stable heat extraction. However, this aspect offers scope for further refinement of the system.

The observed multi-year performance demonstrated cumulative improvement in storage efficiency. The peak sand temperature increased from 59.0 °C in the first cycle to 62.7 °C in the third cycle, while the corresponding maximum heat-loss rate declined from 685.5 W to 587.5 W, respectively. This behaviour indicates that progressive warming of the surrounding soil reduced the boundary temperature gradient, lowering conductive losses and enhancing internal heat retention. Consequently, cumulative annual heat losses decreased from 3309.5 kWh (35.2%) in the first cycle to 2529.1 kWh (26.9%) in the final year. Therefore, these findings emphasize the practical potential of soil-based TES as a cost-effective and sustainable solution for residential heating in cold climates. The synergetic interaction between the TES, insulation, and near-field soil produces a self-stabilizing, repeatable annual operating regime that maximizes the utilization of the 9402 kWh solar input without the need for deep drilling or complex components. The use of locally available sand supports sustainable construction practices and reduces environmental footprint and contributing to the decarbonization of building heating systems.

From the economic analysis, it is clear that different TES technologies present distinct structural and operational requirements that influence their suitability for residential applications. When compared with other seasonal storage solutions, the sand-based TES demonstrates a balanced combination of technical performance and implementation simplicity. ATES and BTES systems generally offer higher storage efficiency but require specialized geological conditions, drilling operations, and more complex infrastructure. Tank-type TES provides excellent thermal control but involves substantially higher construction demands, long-term maintenance needs, material durability constraints, and system complexity. In contrast, the sand-based TES operates with minimal site constraints

and reduced system complexity, while still achieving stable multi-year performance and progressive loss reduction, making it a practical option for residential-scale seasonal storage in cold climates.

In addition to the system-level and techno-economic optimization, future research may also focus on material-level enhancements of thermal accumulators. Recent studies indicate that nano-composite-based heat storage materials, particularly those modified with carbon nanotubes, graphene derivatives, or metallic nanostructures, can significantly enhance effective thermal conductivity and controllability of heat transfer while maintaining energy storage capability. Such advances could improve charging and discharging rates and reduce internal thermal resistance in next-generation thermal energy storage systems. However, challenges related to material cost, long-term thermal stability, scalability, and environmental compatibility currently limit their applications, especially for building-scale and seasonal storage, and therefore require further investigation [77].

Author Contributions: Conceptualization, S.B. and T.Z.; methodology, S.B. and T.Z.; software, S.B. and T.Z.; validation, S.B. and T.Z.; formal analysis, S.B. and T.Z.; investigation, S.B. and T.Z.; resources, S.B. and T.Z.; data curation, S.B. and T.Z.; writing—original draft preparation, S.B. and T.Z.; writing—review and editing, S.B. and T.Z.; visualization, S.B. and T.Z.; supervision, T.Z. All authors have read and agreed to the published version of the manuscript.

Funding: This research received no external funding.

Data Availability Statement: The original contribution presented in this study is included in the article. Further inquiries can be directed to the corresponding author.

Conflicts of Interest: The authors declare no conflicts of interest.

References

1. Renewable Energy Statistics—Statistics Explained. Available online: https://ec.europa.eu/eurostat/statistics-explained/index.php?title=Renewable_energy_statistics (accessed on 13 April 2025).
2. Energy Consumption in Households—Statistics Explained. Available online: https://ec.europa.eu/eurostat/statistics-explained/index.php?title=Energy_consumption_in_households (accessed on 13 April 2025).
3. Greenhouse Gas Emissions from Energy Use in Buildings in Europe | European Environment Agency's Home Page. Available online: https://www.eea.europa.eu/en/analysis/indicators/greenhouse-gas-emissions-from-energy (accessed on 13 April 2025).
4. EU is Wasting Free Energy as Industry Flatlines—POLITICO. Available online: https://www.politico.eu/article/eu-energy-waste-prices-energy-storage (accessed on 13 April 2025).
5. Kittel, M.; Roth, A.; Schill, W.-P. Coping with the Dunkelflaute: Power System Implications of Variable Renewable Energy Droughts in Europe. November 2024. Available online: https://arxiv.org/abs/2411.17683v3 (accessed on 13 April 2025).
6. Pilkington. Solar International GmbH. Survey of Thermal Storage for Parabolic Trough Power Plants; Period of Performance: September 13, 1999–June 12, 2000. 2000. Available online: https://www.osti.gov/biblio/765081 (accessed on 21 September 2025).
7. Pinel, P.; Cruickshank, C.A.; Beausoleil-Morrison, I.; Wills, A. A review of available methods for seasonal storage of solar thermal energy in residential applications. *Renew. Sustain. Energy Rev.* **2011**, *15*, 3341–3359. [CrossRef]
8. Brief, T. IEA-ETSAP and IRENA © Technology Brief E17-Thermal Energy Storage Energy Technology Systems Analysis Programme. 2013. Available online: https://www.irena.org/-/media/Files/IRENA/Agency/Publication/2013/IRENA-ETSAP-Tech-Brief-E17-Thermal-Energy-Storage (accessed on 4 December 2025).
9. SINTEF. *Thermal Energy Storage a State-of-the-Art Smart Energy-Efficient Buildings at NTNU and SINTEF*; SINTEF: Trondheim, Norway, 2002.
10. Cabeza, L.F.; Oró, E. Thermal Energy Storage for Renewable Heating and Cooling Systems. In *Renewable Heating and Cooling: Technologies and Applications*; Woodhead Publishing: Cambridge, UK, 2016; pp. 139–179. [CrossRef]
11. Hariri, A.S.; Ward, I.C. A review of thermal storage systems used in building applications. *Build. Environ.* **1988**, *23*, 1–10. [CrossRef]
12. Zhang, Y.; Xia, C.; Zhou, S.; Peng, W.; Xu, K.; Zhang, J. Experimental and numerical investigations of the energy performance of a solar seasonal thermal storage heating system under different operation modes in cold-region tunnels. *Tunn. Undergr. Space Technol.* **2024**, *154*, 106089. [CrossRef]

13. Gado, M.G.; Palomba, V.; Brancato, V.; Frazzica, A. An innovative intermediate-based sorption thermal energy storage (STES) concept for power-to-heating/cooling purposes in buildings: From experimental dynamics to operational examination. *Energy Convers. Manag.* **2025**, *327*, 119584. [CrossRef]
14. Xu, G.; Hu, L.; Luo, Y.; Tian, Z.; Deng, J.; Yuan, G.; Fan, J. Numerical modeling and parametric analysis of thermal performance for the large-scale seasonal thermal energy storage. *Energy Build.* **2022**, *275*, 112459. [CrossRef]
15. Rostampour, V.; Keviczky, T. Probabilistic Energy Management for Building Climate Comfort in Smart Thermal Grids with Seasonal Storage Systems. *IEEE Trans. Smart Grid* **2016**, *10*, 3687–3697. [CrossRef]
16. Marojević, K.; Kurevija, T.; Macenić, M. Challenges and Opportunities for Aquifer Thermal Energy Storage (ATES) in EU Energy Transition Efforts—An Overview. *Energies* **2025**, *18*, 1001. [CrossRef]
17. Possemiers, M.; Huysmans, M.; Batelaan, O. Influence of Aquifer Thermal Energy Storage on groundwater quality: A review illustrated by seven case studies from Belgium. *J. Hydrol. Reg. Stud.* **2014**, *2*, 20–34. [CrossRef]
18. Song, W.; Harzer, J.; Jung, C.; Sander, L.; Diehl, M. Numerical Method for Simultaneous Design and Control Optimization of Seasonal Thermal Energy Storage Systems. January 2025. Available online: https://arxiv.org/abs/2501.07427v1 (accessed on 14 April 2025).
19. Lanahan, M.; Tabares-Velasco, P.C. Seasonal thermal-energy storage: A critical review on BTES systems, modeling, and system design for higher system efficiency. *Energies* **2017**, *10*, 743. [CrossRef]
20. Kerskes, H. *Experimental and Numerical Investigations on Thermo Chemical Heat Storage*; University Stuttgart: Stuttgart, Germany, 2016; pp. 1–10. [CrossRef]
21. Abdullah, M.; Koushaeian, N.; Shah, A.; Chung, J.D. A review on thermochemical seasonal solar energy storage materials and modeling methods. *Int. J. Air Cond. Refrig.* **2024**, *32*, 1–26. [CrossRef]
22. Ali, E.; Ajbar, A.; Lamrani, B. Numerical Investigation of Thermal Energy Storage Systems for Collective Heating of Buildings. *Buildings* **2024**, *14*, 141. [CrossRef]
23. Arslan, B.; Ilbas, M. Experimental and Numerical Investigation of Macroencapsulated Phase Change Materials for Thermal Energy Storage. *Materials* **2024**, *17*, 2804. [CrossRef]
24. Morciano, M.; Fasano, M.; Chiavazzo, E.; Mongibello, L. Trending applications of Phase Change Materials in sustainable thermal engineering: An up-to-date review. *Energy Convers. Manag. X* **2025**, *25*, 100862. [CrossRef]
25. Hua, W.; Lv, X.; Zhang, X.; Ji, Z.; Zhu, J. Research progress of seasonal thermal energy storage technology based on supercooled phase change materials. *J. Energy Storage* **2023**, *67*, 107378. [CrossRef]
26. Yang, Z.L.; Walvekar, R.; Wong, W.P.; Sharma, R.K.; Dharaskar, S.; Khalid, M. Advances in phase change materials, heat transfer enhancement techniques, and their applications in thermal energy storage: A comprehensive review. *J. Energy Storage* **2024**, *87*, 111329. [CrossRef]
27. Pourasl, H.H.; Barenji, R.V.; Khojastehnezhad, V.M. Solar energy status in the world: A comprehensive review. *Energy Rep.* **2023**, *10*, 3474–3493. [CrossRef]
28. Ergun, S.; Dik, A.; Boukhanouf, R.; Omer, S. Large-Scale Renewable Energy Integration: Tackling Technical Obstacles and Exploring Energy Storage Innovations. *Sustainability* **2025**, *17*, 1311. [CrossRef]
29. Jiang, H.; Luo, J.; Guo, Y.; Du, E.; Zhang, N.; Fang, Y.; Wang, Y.; Strbac, G. Modeling seasonal thermal storage dynamics in the year-round scheduling of renewable energy systems. *Appl. Energy* **2025**, *379*, 124828. [CrossRef]
30. Brites, G.J.; Garruço, M.; Fernandes, M.S.; Pinto, D.M.S.; Gaspar, A.R. Seasonal storage for space heating using solar DHW surplus. *Renew. Energy* **2024**, *231*, 120889. [CrossRef]
31. Antoniadis, C.N.; Martinopoulos, G. Optimization of a building integrated solar thermal system with seasonal storage using TRNSYS. *Renew. Energy* **2019**, *137*, 56–66. [CrossRef]
32. Yang, T.; Liu, W.; Kramer, G.J. Seasonal thermal energy storage employing solar heat: A case study of Heilongjiang, China, exploring the transition to clean heating and renewable power integration. *Energy* **2024**, *305*, 132334. [CrossRef]
33. Rostampour, V.; Jaxa-Rozen, M.; Bloemendal, M.; Keviczky, T. Building Climate Energy Management in Smart Thermal Grids via Aquifer Thermal Energy Storage Systems. *Energy Procedia* **2016**, *97*, 59–66. [CrossRef]
34. Bolton, R.; Cameron, L.; Kerr, N.; Winskel, M.; Desguers, T. Seasonal thermal energy storage as a complementary technology: Case study insights from Denmark and the Netherlands. *J. Energy Storage* **2023**, *73*, 109249. [CrossRef]
35. Madiraju, K.S. The Canadian Context: Energy. In *Global Sustainable Communities Handbook: Green Design Technologies and Economics*; Elsevier: Amsterdam, The Netherlands, 2014; pp. 255–291. [CrossRef]
36. Sadeghi, H.; Jalali, R.; Singh, R.M. A review of borehole thermal energy storage and its integration into district heating systems. *Renew. Sustain. Energy Rev.* **2024**, *192*, 114236. [CrossRef]
37. Rathore, P.K.S.; Sikarwar, B.S. Thermal energy storage using phase change material for solar thermal technologies: A sustainable and efficient approach. *Sol. Energy Mater. Sol. Cells* **2024**, *277*, 113134. [CrossRef]
38. Liu, K.; Wu, C.; Gan, H.; Liu, C.; Zhao, J. Latent heat thermal energy storage: Theory and practice in performance enhancement based on heat pipes. *J. Energy Storage* **2024**, *97*, 112844. [CrossRef]

39. Goel, V.; Dwivedi, A.; Kumar, R.; Kumar, R.; Pandey, A.K.; Chopra, K.; Tyagi, V.V. PCM-assisted energy storage systems for solar-thermal applications: Review of the associated problems and their mitigation strategies. *J. Energy Storage* **2023**, *69*, 107912. [CrossRef]
40. Zhao, C.; Yan, J.; Tian, X.; Xue, X.; Zhao, Y. Progress in thermal energy storage technologies for achieving carbon neutrality. *Carbon Neutrality* **2023**, *2*, 10. [CrossRef]
41. Steinmann, W.-D. Thermochemical Energy Storage. In *Thermal Energy Storage for Medium and High Temperatures*; Springer: Berlin/Heidelberg, Germany, 2022; pp. 241–262. [CrossRef]
42. *ISO 9806:2017*; Solar Energy—Solar Thermal Collectors—Test Methods. International Organization for Standardization (ISO): Geneva, Switzerland, 2017. Available online: https://www.iso.org/standard/67978.html (accessed on 11 December 2025).
43. JRC Photovoltaic Geographical Information System (PVGIS)—European Commission. Available online: https://re.jrc.ec.europa.eu/pvg_tools/en/ (accessed on 25 July 2025).
44. María, A.; Huld, G.T. *Performance Comparison of Different Models for the Estimation of Global Irradiance on Inclined Surfaces*; European Commission: Brussels, Belgium, 2013. [CrossRef]
45. PVGIS Data Sources & Calculation Methods—European Commission. Available online: https://joint-research-centre.ec.europa.eu/photovoltaic-geographical-information-system-pvgis/getting-started-pvgis/pvgis-data-sources-calculation-methods (accessed on 27 July 2025).
46. Kalogirou, S.A. Solar thermal collectors and applications. *Prog. Energy Combust. Sci.* **2004**, *30*, 231–295. [CrossRef]
47. *EN 12975-1:2006*; Thermal Solar Systems and Components—Solar Collectors—Part 1: General. iTeh Standards: San Francisco, CA, USA, 2006. Available online: https://standards.iteh.ai/catalog/standards/cen/56f8d8b4-543c-45ee-aefc-2dc4b3acd92a/en-12975-1-2006 (accessed on 20 August 2025).
48. Kramer, K.S.; Mehnert, S.; Geimer, K.; Thoma, C.; Fahr, S.; Ollas, P. *Guide to Standard ISO 9806:2017 A Resource for Manufacturers, Testing Laboratories, Certification Bodies and Regulatory Agencies*; ISO: Geneva, Switzerland, 2018. [CrossRef]
49. Heat Transfer Fluids for Solar Water Heating Systems | Department of Energy. Available online: https://www.energy.gov/energysaver/heat-transfer-fluids-solar-water-heating-systems (accessed on 31 March 2025).
50. Fan, J.; Shah, L.J.; Furbo, S. Flow distribution in a solar collector panel with horizontally inclined absorber strips. *Sol. Energy* **2007**, *81*, 1501–1511. [CrossRef]
51. Applications: Tube, Pipe & Fittings: Copper Tube Handbook: III. Solar Energy Systems. Available online: https://copper.org/applications/plumbing/cth/design-installation/cth_3design_solar.php (accessed on 19 July 2025).
52. Liu, H.; Wang, D.; Liu, Y.; Li, Y.; Gao, M.; Fan, J.; Wei, M.; Liu, L. General rights Thermal storage and loss characteristics of underground water pits of solar district heating systems in Xizang Plateau, China. *Energy* **2024**, *308*, 132702. [CrossRef]
53. Zdankus, T.; Bandarwadkar, S.; Vaiciunas, J.; Stelmokaitis, G.; Vaicaitis, A. Research on Increasing the Building's Energy Efficiency by Using the Ground Beneath It for Thermo-Accumulation. *Sustainability* **2025**, *17*, 262. [CrossRef]
54. Verma, S.; Kelsall, C.; Buznitsky, K.; LaPotin, A.; Sandeep, A.; Henry, A. Designing for Effective Heat Transfer in a Solid Thermal Energy Storage System. 2024. Available online: https://arxiv.org/pdf/2402.07764 (accessed on 28 September 2025).
55. Home—Lithuanian Geological Survey Under Ministry of Environment. Available online: https://lgt.lrv.lt/en/ (accessed on 18 June 2025).
56. Abu-Hamdeh, N.H.; Reeder, R.C. Soil Thermal Conductivity Effects of Density, Moisture, Salt Concentration, and Organic Matter. *Soil. Sci. Soc. Am. J.* **2000**, *64*, 1285–1290. [CrossRef]
57. Copper—Density, Specific Heat and Thermal Conductivity vs. Temperature. Available online: https://www.engineeringtoolbox.com/copper-density-specific-heat-thermal-conductivity-vs-temperature-d_2223.html (accessed on 22 September 2025).
58. Poly Foam: Middle East LLC: Phenolic Foam—Poly Foam. Available online: https://polyfoamme.com/phenolic-foam/ (accessed on 25 October 2025).
59. Song, Y.; Du, A.; Cui, T. Using the Degree-Day Method to Analyze Central Heating Energy Consumption in Cities of Northern China. *Sustainability* **2024**, *16*, 1008. [CrossRef]
60. Pan, X.; Xiang, Y.; Gao, M.; Fan, J.; Furbo, S.; Wang, D.; Xu, C. Long-term thermal performance analysis of a large-scale water pit thermal energy storage. *J. Energy Storage* **2022**, *52*, 105001. [CrossRef]
61. Kotzur, L.; Markewitz, P.; Robinius, M.; Stolten, D. Time series aggregation for energy system design: Modeling seasonal storage. *Appl. Energy* **2018**, *213*, 123–135. [CrossRef]
62. Housing—Oficialiosios Statistikos Portalas. Available online: https://osp.stat.gov.lt/en/lietuvos-statistikos-metrastis/lsm-2019/gyventojai-ir-socialine-statistika/bustas (accessed on 31 March 2025).
63. Technical Regulations for Construction, STR 2.01.02:2016, Energy Performance Design and Certification of Buildings. Available online: https://e-seimas.lrs.lt/portal/legalAct/lt/TAD/15767120a80711e68987e8320e9a5185/asr (accessed on 25 April 2025).
64. Technical Regulations for Construction, STR 2.01.12:2024, Construction Climatology. Available online: https://e-seimas.lrs.lt/portal/legalAct/lt/TAD/60c1acd17f6311ef84ff9693ecd03ff5?jfwid=e5xndzg76 (accessed on 25 April 2025).

65. Kupiec, K.; Król, B.; Kupiec, K.; Król, B. Optimal Collector Tilt Angle to Maximize Solar Fraction in Residential Heating Systems: A Numerical Study for Temperate Climates. *Sustainability* **2025**, *17*, 6385. [CrossRef]
66. Alvarez, A.; Pate, M.B. Design Optimization of Solar-Collector Tilt Angle for Annual-Maximum and Seasonal-Balanced Energy Received. *J. Sol. Energy Eng.* **2025**, *147*, 021009. [CrossRef]
67. Stanciu, C.; Stanciu, D. Optimum tilt angle for flat plate collectors all over the World—A declination dependence formula and comparisons of three solar radiation models. *Energy Convers. Manag.* **2014**, *81*, 133–143. [CrossRef]
68. Sunrise and Sunset Times in Kaunas. Available online: https://www.timeanddate.com/sun/lithuania/kaunas (accessed on 27 October 2025).
69. *ISO 13370:2017*; Thermal Performance of Buildings—Heat Transfer via the Ground—Calculation Methods. International Organization for Standardization (ISO): Geneva, Switzerland, 2017. Available online: https://www.iso.org/standard/65716.html (accessed on 11 December 2025).
70. OshKosh B'gosh Brand Profile U.S. 2022—Statista. Available online: https://www.statista.com/forecasts/1252024/oshkosh-b-gosh-toys-and-baby-online-shops-brand-profile-in-the-united-states (accessed on 5 December 2025).
71. Kingspan Kooltherm—Phenolic Foam Insulation Board. Available online: https://materialsmarket.com/insulation/material-type/phenolic-insulation (accessed on 5 December 2025).
72. Construction Cost of New Residential Buildings. Available online: https://ec.europa.eu/eurostat/databrowser/view/teiis510/default/table (accessed on 5 December 2025).
73. Thermal Energy Storage. Available online: https://www.irena.org/Publications/2013/Jan/Thermal-energy-storage (accessed on 5 December 2025).
74. Barrios, M.; Blum, P. Evaluation of an Aquifer Thermal Energy Storage (ATES) for the City Hospital in Karlsruhe (Germany). Master's Thesis, Karlsruhe Institute of Technology (KIT), Karlsruhe, Germany, 2015.
75. Schmidt, T. Solar District Heating Guidelines. 2012. Available online: www.solar-district-heating.eu (accessed on 7 December 2025).
76. Lüchinger, R.; Hendry, R.; Walter, H.; Worlitschek, J.; Schuetz, P. Cost Analysis for Large Thermal Energy Storage Systems. *J. Eng. Sustain. Build. Cities* **2025**, *6*, 021006. [CrossRef]
77. Shchegolkov, A.; Shchegolkov, A.; Demidova, A. The use of nanomodified heat storage materials for thermal stabilization in the engineering and aerospace industry as a solution for economy. In Proceedings of the MATEC Web of Conferences, EDP Sciences, Sevastopol, Russia, 30 October 2018. [CrossRef]